

# Non-linear evolution and acceleration of unstable fuel-lean hydrogen/air flame at ambient and cryogenic temperatures

Linlin Yang<sup>a,c</sup>, Tianhan Zhang<sup>b</sup>, Yiqing Wang<sup>a</sup>, Xiaohang Fang<sup>c,d</sup>, Felix Leach<sup>c</sup>, Zheng Chen<sup>a,\*</sup>

<sup>a</sup>*College of Engineering, Peking University, Beijing, 100871, China*

<sup>b</sup>*AI for Science Institute, Beijing, 100080, China*

<sup>c</sup>*Department of Engineering Science, University of Oxford, Oxford, OX1 3PJ, UK*

<sup>d</sup>*Department of Mechanical & Manufacturing Engineering, Schulich School of Engineering, University of Calgary, Calgary, T2L 1Y6, Canada*

---

## Abstract

Hydrogen storage at cryogenic temperatures is crucial for industrial applications, yet these conditions can significantly affect flame behavior. Both Darrieus-Landau instability (DLI) and diffusional-thermal instability (DTI) can intensify at cryogenic temperature, leading to unique flame dynamics relevant to safe hydrogen usage. In this study, two-dimensional simulations are performed to assess the effects of cryogenic temperature on the non-linear evolution and acceleration of fuel-lean hydrogen/air flames. By changing the initial temperature and equivalence ratio of the unburned gas as well as the channel width, distinct flame evolution regimes driven by the interplay of DLI and DTI are identified. Specifically, for fuel-lean hydrogen/air flames, the growth rate of DLI and DTI in the linear stage increases at cryogenic temperatures. In the non-linear stage, DTI leads to the chaotic evolution of the cellular flame, which is further destabilized at cryogenic temperatures. It is found that the long-term dynamics, characterized by cell splitting, merging, and lateral movement, result from complex interactions among flow, flame stretch, and chemical reactions. Moreover, flame structure analysis shows that, compared to ambient temperatures, cryogenic temperatures significantly increase the local reaction rate. The propagation speed of fuel-lean

---

\*Corresponding Author

*Email address:* cz@pku.edu.cn (Zheng Chen)

hydrogen/air flames is further accelerated at cryogenic temperature, which is associated with the combined effects of enhanced local reaction rate and increased flame surface area, with the primary contribution from enhanced DTI and the secondary contribution from enhanced DLI. In contrast, stoichiometric and fuel-rich flames propagate in a stable single-cusp shape, with their acceleration primarily driven by DLI and flame surface area increase. The width of the channel also affects cellular flame evolution. Rather than altering reaction rates, channel geometry influences flame acceleration mainly through constraining the surface area during flame propagation. These insights contribute to our understanding of cryogenic hydrogen flame dynamics and have important implications for hydrogen safety management.

*Keywords:* Hydrogen flame, Cryogenic temperature, Cellular instabilities, Non-linear evolution

---

## **Novelty and Significance Statement**

The novelty of this study lies in assessing and interpreting the effects of cryogenic temperatures on fuel-lean hydrogen/air flames subjected to both Darrieus-Landau instability (DLI) and diffusional-thermal instability (DTI) for the first time. Through detailed numerical simulations, we reveal mechanisms driving the chaotic evolution and cellular structure of flame fronts under cryogenic conditions. Our quantitative analysis demonstrates the relative contributions of DLI and DTI. The research fills a critical knowledge gap by examining the role of DLI and DTI at cryogenic conditions for highly unstable fuel-lean hydrogen/air flame. The results are especially valuable for predicting and managing potential flame acceleration hazards in cryogenic hydrogen systems, where traditional ambient-temperature models may not adequately capture the underlying physics.

## **Author Contributions Statement**

- L. Yang: Conceptualization, Methodology and formal analysis, Writing – original draft, Writing – review & editing
- T. Zhang: Assisted in further analysis, Writing – review & editing.
- Y. Wang: Assisted in further analysis, Writing – review & editing.

- X. Fang: Assisted in further analysis, Funding acquisition, Writing – review & editing.
- F. Leach: Assisted in further analysis, Funding acquisition, Writing – review & editing.
- Z. Chen: Conceptualization, Methodology, Writing –review & editing, Funding acquisition, Supervision.

## 1. Introduction

Recently, hydrogen has received great attention for its potential to reduce carbon dioxide emissions [1, 2]. Cryogenic storage and hydrogen transportation are necessary for some applications due to gaseous hydrogen’s low volumetric energy density. Due to the low minimum ignition energy and high diffusivity and reactivity, safety issues related to cryogenic hydrogen pose a serious problem to hydrogen utilization [3]. After accidental release, liquid hydrogen can evaporate rapidly and mix with ambient air [4], forming a cryogenic premixed hydrogen/air mixture, leading to possible deflagration after ignition [5]. Moreover, the onset of flame instabilities may lead to the deflagration-to-detonation transition (DDT) through flame acceleration, causing faster energy release and more severe damage [6–8]. Therefore, it is important to understand the propagation and acceleration of hydrogen/air flames subject to instabilities at cryogenic temperatures.

In the absence of gravity [9], intrinsic flame front instabilities including Darrieus-Landau instability (DLI, or hydrodynamic instability) and diffusional-thermal instability (DTI) [10–13], can greatly accelerate the flame propagation through flame front wrinkling. Under cryogenic conditions, the DLI can be enhanced as the expansion ratio (density ratio of unburned to burned gas, i.e.,  $\sigma = \rho_u/\rho_b$ ) becomes large [14]. The DTI can also become significant since the Zel’dovich number increases with decreasing temperature for fuel-lean hydrogen/air flames with sub-unity Lewis number ( $Le < 1$ ) [11, 15]. Previous studies [7, 16, 17] demonstrated that DLI at cryogenic temperatures can be much stronger than that at ambient temperatures for stoichiometric hydrogen/air flame. For turbulent flames, the effect of DLI on flame acceleration was studied by Chen *et al.* [18]. These studies show that a large expansion ratio at cryogenic temperatures causes strong flame acceleration. In the recent work by Missey *et al.* [19], the impact of fuel stratification on the propagation of cryogenic fuel-lean flame above a liquid hydrogen pool was analyzed. They found that flame instabilities play a role in flame kernel development in the early stage. However, the impact of instabilities on long-term flame propagation and acceleration was not thoroughly discussed. For fuel-lean hydrogen/air flames at cryogenic temperatures, the combined effects of DLI and DTI may lead to even stronger flame acceleration, posing risks to the safe use of hydrogen. In the literature, there is a lack of quantitative analysis on the effects of DLI and DTI on the evolution and acceleration of cryogenic fuel-lean hydrogen/air flame, which inspires the present study.

1        There are several theoretical studies on linear instabilities development  
2 for planar flame [20, 21], circular expanding flame [22], and spherical ex-  
3 panding flame [23]. However, for fuel-lean hydrogen/air flames, Frouzakis *et*  
4 *al.* [24] have shown that linear theory fails to predict the dispersion relation.  
5 In addition, the non-linear evolution of wrinkled flames is more relevant to  
6 practical applications since linear evolution only lasts for a relatively short  
7 interval. Although analytical theory [25, 26] on the non-linear evolution of  
8 unstable flames has been developed, it cannot be readily applied to cryogenic  
9 flame evolution due to the strong assumption of weak thermal expansion. To  
10 account for realistic thermal expansion, a modified model in the context of  
11 hydrodynamic theory [27, 28] has been developed. However, the modified  
12 model requires numerical treatment, and the internal structure of the flame  
13 front is greatly simplified. Therefore, numerical research is still needed to  
14 study the evolution and acceleration of the fuel-lean hydrogen/air flames at  
15 cryogenic temperatures.

16        Various numerical studies in the literature have focused on the evolution  
17 of premixed hydrogen/air flames at ambient temperatures [29–34]. Berger *et*  
18 *al.* [15] investigated the effects of pressure, equivalence ratio, and temperature  
19 on premixed hydrogen/air flame instabilities in the linear stages. They found  
20 that intrinsic instabilities can be enhanced by decreasing the equivalence ratio  
21 and the temperature of the unburnt gas or by increasing the pressure. Later  
22 on, they studied the non-linear evolution of unstable hydrogen/air flames  
23 subjected to instabilities including DLI and DTI [31]. Their results showed  
24 that the instability development in the non-linear stage is affected by equiv-  
25 alence ratio, initial temperature, and pressure in the same manner as that  
26 in the linear stage in [15]. A recent study by Attili *et al.* [35] suggested that  
27 pressure can affect the development of DLI through different mechanisms. In  
28 addition, the contribution of DLI and DTI, as well as the synergistic interac-  
29 tion between DLI and DTI on flame evolution, was investigated numerically  
30 by Berger *et al.* [36]. However, none of the studies mentioned above covered  
31 the cryogenic temperature range. The impact of cryogenic temperatures on  
32 fuel-lean hydrogen/air flame evolution and accelerative propagation remains  
33 unclear. This motivates the present study, which focuses on the instability  
34 development of cryogenic fuel-lean hydrogen/air flames.

35        Given the background mentioned above, this study aims to investigate the  
36 fuel-lean hydrogen/air flame propagation subjected to intrinsic instabilities at  
37 cryogenic temperatures, focusing on the long-term non-linear evolution and  
38 acceleration associated with strong DLI and DTI. The paper is organized as

1 follows. Section 2 provides an overview of the numerical models and details  
 2 on the setup. Then, Section 3 presents the simulation results and discusses  
 3 various factors affecting the propagation and acceleration of fuel-lean flames.  
 4 Finally, Section 4 summarizes the findings of this study.

## 5 2. Numerical model and methods

6 We consider premixed hydrogen/air flame propagation in a two-dimensional  
 7 rectangular channel, as shown in Fig. 1. This configuration has been used to  
 8 study flame instabilities [24, 29, 36]. The flame propagates from the right end  
 9 to the left. Periodic boundary conditions are imposed on the top and bot-  
 10 tom of the domain, while inflow and outflow boundary conditions are applied  
 11 to the left and right boundaries, respectively. Note that periodic boundary  
 12 conditions, rather than wall boundary conditions, are employed to prevent  
 13 the flame quenching, which could otherwise affect the development of flame  
 14 instabilities.

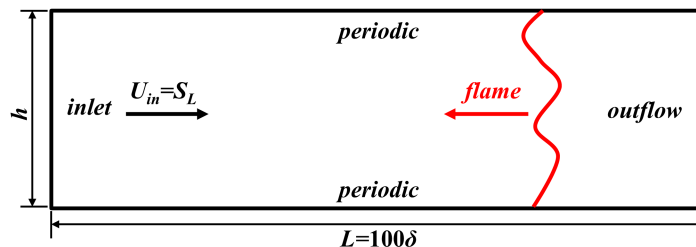


Figure 1: Schematic of the computational domain for the planar  $H_2$ /air flame propagating towards the left inlet.

15 We consider factors affecting the flame instabilities, including equivalence  
 16 ratio  $\phi$ , initial temperature  $T_0$ , and channel width  $h$ . Although the fuel-  
 17 lean hydrogen/air mixtures with the equivalence ratio of  $\phi=0.5$  and initial  
 18 temperatures of  $T_0 = 100$  K and 300 K are the focus of this study, simulations  
 19 with  $\phi=1.0$  and  $\phi=2.5$  are conducted to evaluate the effect of DLI alone, as  
 20 shown in Table 1.

21 The channel width depends on the equivalence ratio and temperature of  
 22 the mixture. The length of the computational domain is fixed to  $L = 100\delta$ ,  
 23 where  $\delta$  is the flame thickness of the corresponding 1D premixed planar  
 24 flame. It is determined by the maximum temperature gradient, i.e.,  $\delta =$   
 25  $(T_b - T_0)/(dT/dx)_{max}$ . Here  $T_b$  and  $T_0$  are the temperatures of burned and

Table 1: Cases with different initial temperatures ( $T_0$ ) and equivalence ratios ( $\phi$ ) considered in this study.

cases	$\phi = 0.5$	$\phi = 1$	$\phi = 2.5$
$T_0 = 100$ K	DLI&DTI	DLI	weak DLI
$T_0 = 300$ K	DLI&DTI	DLI	weak DLI

1 unburned gases, respectively. Cantera [37] is used to calculate 1D unstretched  
 2 planar flame parameters, such as laminar flame speed  $S_L$  and flame thickness  
 3  $\delta$ . The width of the computational domain varies by case, and a series of  
 4 values are considered:  $h=4\delta$ ,  $5\delta$ ,  $6\delta$ ,  $8\delta$ ,  $10\delta$ ,  $40\delta$ , and  $100\delta$ . According  
 5 to a previous study [30], for unstable hydrogen/air flames, a large domain  
 6 ( $h > 25\delta$ ) is necessary to ensure that the channel width does not constrain the  
 7 development of instabilities. Note that the flame is stable for channels with  
 8  $h < 4\delta$ , and the flame front remains planar without wrinkling. Therefore,  
 9 these channel widths, unaffected by flame instabilities, are not considered in  
 10 the present study.

11 The domain is initialized by the corresponding 1D flame profile, and the  
 12 flame front is located at  $x = 90\delta$ . The unburned gas velocity from the inlet  
 13 is  $S_L$ . By imposing small sinusoidal perturbations on the flame front, the  
 14 flame propagates towards the inlet due to the development of instabilities.  
 15 As adopted in the previous study [24], here we also take the perturbation  
 16 amplitude as  $A(t = 0) = 0.001\delta$ , and the wavelength  $\lambda$  is set to be the  
 17 channel width ( $\lambda = h$ ) for different cases. In the following section, unless  
 18 otherwise specified, the length and time scales are normalized by  $\delta$  and  $\delta/S_L$ ,  
 19 respectively.

20 The low-Mach number solver, PeleLM [38], is used to solve the Navier-  
 21 Stokes equations for multi-component reactive flow in the low-Mach number  
 22 limit. The detailed chemical mechanism developed by Konnov [39] and the  
 23 mixture-averaged transport model are considered in the simulations. This  
 24 mechanism was used in previous studies [14, 16] to simulate cryogenic hy-  
 25 drogen/air flame propagation. It is also found that results are insensitive to  
 26 cryogenic temperatures [40]. The Soret diffusion effect is neglected in the  
 27 simulations as previous studies [41–43] have shown that it does not lead to  
 28 qualitative change to hydrogen flames and that its importance appears nearly  
 29 constant from  $T_0 = 300$  K to 100 K [44]. To perform the simulation efficiently,  
 30 adaptive mesh refinement is employed with a base grid size of  $\Delta x = \delta/4$ . The

1 reaction front is consistently resolved using a fine grid with a minimum size  
 2 of  $\Delta x = \delta/32$  throughout the simulation. This grid is fine enough to resolve  
 3 the thin flame front and avoid numerical noise [24, 27], which was considered  
 4 to be a major factor that affects the evolution of large-scale flames [45]. Af-  
 5 ter a short period of linear evolution, the chaotic evolution in the non-linear  
 6 stage happens, which will be analyzed and discussed in the following section.

### 7 **3. Results and discussion**

#### 8 *3.1. Linear evolution of the fuel-lean $H_2$ /air flames*

9 Due to the unstable nature of the fuel-lean hydrogen/air flame, initial  
 10 perturbations imposed on the flame front grow exponentially in the linear  
 11 stage. We first examine the dispersion relation in the preceding linear stage  
 12 to better understand non-linear flame evolution. The numerical growth rate  
 13 is calculated based on the rate of perturbation amplitude  $A(t)$  [2, 15, 46],  
 14 i.e.,

$$\omega^* = \frac{1}{A(t)} \frac{dA(t)}{dt} = \frac{d \ln[A(t)]}{dt} \quad (1)$$

15 As mentioned above, the growth rate and wavenumber are normalized  
 16 by corresponding 1D unstretched planar flame parameters, the normalized  
 17 growth rate  $\omega$  and wavenumber  $k$  are

$$\omega = \omega^* \delta / S_L, k = k^* \delta = 2\pi \delta / h \quad (2)$$

18 The dispersion relation for lean premixed hydrogen flames at  $T_0 = 100$  K  
 19 and 300 K is shown in Fig. 2. To compare with results in the literature, data  
 20 for the case at  $\phi=0.5$  and  $T_0 = 300$  K extracted from [24] are also plotted in  
 21 Fig. 2. It is seen that results for  $T_0 = 300$  K are close to the results in [24].  
 22 Considering the difference in chemical reaction mechanisms, good agreement  
 23 is achieved between these results and the literature.

24 As shown in Fig. 2, the cryogenic condition significantly impacts flame  
 25 instability development in the linear stage. The normalized growth rate  $\omega$   
 26 increases greatly at cryogenic temperatures of  $T_0 = 100$  K. The maximum  
 27 normalized growth rate at  $T_0 = 300$  K ( $\omega = 1.2$ ) is much smaller than the  
 28 maximum normalized growth rate at  $T_0 = 100$  K ( $\omega = 3.5$ ). As discussed  
 29 in [15], a larger maximum growth rate implies stronger flame instability.

1 Therefore, the flame instability is greatly enhanced at cryogenic tempera-  
 2 tures. Note that the flame instability in the non-linear stage is relevant to  
 3 the maximum growth rate in the linear stage [15, 31]. Therefore, the cryo-  
 4 genic temperatures are expected to affect the non-linear evolution of unstable  
 5 flame. On the other hand, for each normalized wavenumber  $k$  smaller than  
 6 the cut-off wavenumber at which the growth rate is zero,  $\omega$  for  $T_0 = 100$  K  
 7 is always larger than that for  $T_0 = 300$  K, indicating that perturbations in  
 8 the range of unstable wavenumber grow faster at cryogenic temperatures.

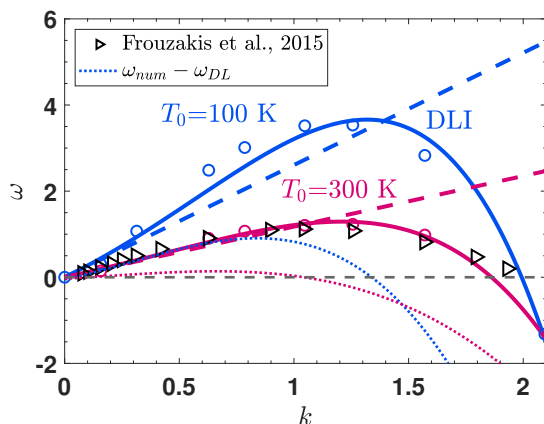


Figure 2: Dispersion relation for premixed  $H_2$ /air flames at  $\phi=0.5$ ,  $T_0 = 100$  K and 300 K. The circles correspond to the numerical growth rate in this study. The solid curves are splines fitting these numerical growth rates according to Eq.(3). The black triangles refer to data extracted from [24]. Dashed lines are the theoretical growth rate of DLI. The dotted lines are the differences between the numerical and theoretical growth rates.

9 In the literature, the growth rate of lean flame is fitted by a fourth-order  
 10 polynomial [15, 47] in the form:

$$\omega_{fit} = \omega_{DL}k + \Pi_2k^2 - \Pi_4k^4 \quad (3)$$

11 where  $\omega_{DL}$  is the expression of the theoretical growth rate of DLI [10, 11, 29]:

$$\omega_{DL} = \frac{1}{\sigma + 1}(\sqrt{\sigma^3 + \sigma^2 - \sigma - \sigma} - \sigma) \quad (4)$$

12 It is noted that in Eq.(3), there is no constraint on the coefficient  $\Pi_2$ ,  
 13 while the coefficient  $\Pi_4$  must be positive to suppress the growth of short  
 14 wavelength perturbations. The fitting coefficients according to Eq.(3) are  
 15 listed in Table 2. To assess the individual effect of DLI, we also plot the

1 contribution of DLI for ambient and cryogenic flames based on Eq.(4), as  
 2 denoted by the dashed lines in Fig. 2. It is seen that the growth rate of  
 3 DLI,  $\omega_{DL}$ , is larger at lower initial temperatures, indicating enhanced DLI  
 4 at cryogenic temperatures.

5 On the other hand, the differences between numerical growth rate and  
 6 theoretical growth rate are calculated and plotted in Fig. 2 to evaluate the  
 7 contribution of DTI, as shown by the dotted lines. It is found that the growth  
 8 rate due to DTI is also larger at lower initial temperatures. Additionally,  
 9 in Table 2 the coefficient  $\Pi_2$  for  $T_0 = 100$  K is much larger than that for  
 10  $T_0 = 300$  K. Since  $\Pi_2$  is relevant to the effect of DTI, this also shows that  
 11 DTI is enhanced due to the cryogenic conditions. Therefore, at cryogenic  
 12 temperatures, not only is DLI enhanced, but DTI is also enhanced.

Table 2: Comparison of fitting coefficients for  $T_0 = 100$  K and 300 K.

case	$\omega_{DL}$	$\Pi_2$	$\Pi_4$
$T_0 = 100$ K	2.61	1.25	0.64
$T_0 = 300$ K	1.18	0.31	0.27

13 Although this dispersion relation is derived from the linear stage of flame  
 14 evolution, it provides a reasonable estimate for the instability in the non-  
 15 linear stage, as suggested by [15, 31]. Therefore, it is expected that in the  
 16 non-linear stage, both DLI and DTI will also be greatly enhanced at cryogenic  
 17 conditions for the fuel-lean premixed hydrogen/air flame.

### 18 3.2. Non-linear evolution of flame front propagation

19 The linear stage only lasts for a short interval. After a quick transi-  
 20 tion, the unstable flame evolution changes from the linear to the non-linear  
 21 stage, characterized by complicated long-term dynamics of cellular structure  
 22 evolution, including cell splitting, cell merging, and lateral movement [29].  
 23 Figure 3 shows the evolution of the lean flame ( $\phi=0.5$ ) front in the channel  
 24 of  $h = 10\delta$  for  $T_0 = 100$  K and  $T_0 = 300$  K. As flame instabilities develop,  
 25 the flame surface area increases, and the flame propagates towards the un-  
 26 burnt gas on the left side. It is found that the perturbed sinusoidal flame  
 27 quickly transitions to the non-linear evolution stage with two cusps on the  
 28 front. During the flame propagation process, the shape of the flame front  
 29 changes occasionally. For  $T_0 = 100$  K shown in Fig. 3(a), the depth of the

1 two cusps is different after the planar flame changes to the two-cusp regime.  
 2 The two-cusp flame front rapidly evolves to the single-cusp front at around  
 3  $x/\delta=75$ . Then, the flame propagates forwards in this single-cusp regime for  
 4 a long time with lateral movement. During this process, a double-cusp flame  
 5 front appears occasionally with a relatively short lifetime.

6 The evolution of the ambient flame at  $T_0 = 300$  K is different. As shown  
 7 in Fig. 3(b), the flame shape changes from the two-cusp regime to the single-  
 8 cusp regime at around  $x/\delta=60$ . This structure lasts a short interval, then  
 9 transitions to the two-cusp regime at around  $x/\delta=58$ . However, this regime  
 10 is unstable, and it reverts to the single-cusp regime. Finally, the flame moves  
 11 towards the inlet in a single-cusp regime. The comparison between  $T_0 =$   
 12  $100$  K and  $T_0 = 300$  K demonstrates that the lateral movement is more  
 13 pronounced, and the cusp is deeper for the cryogenic flame, which is thereby  
 14 more unstable.

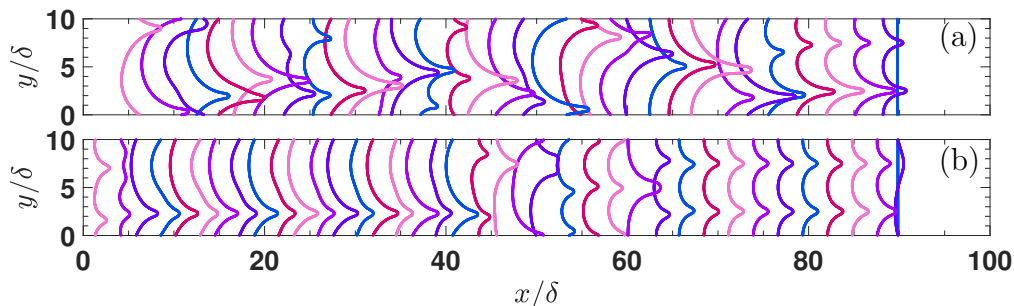


Figure 3: Temporal evolution of flame front propagating in a channel with  $h = 10\delta$  for (a)  $T_0 = 100$  K,  $\phi=0.5$ , (b)  $T_0 = 300$  K,  $\phi=0.5$ . The flame propagates from the right to the left.

15 The flame front evolution for the stoichiometric case ( $\phi=1$ ) is shown in  
 16 Fig. 4. It is noted that for the hydrogen/air mixture at  $\phi=1$ , the effective  
 17 Lewis number is slightly larger than unity, i.e.,  $Le_{eff} > 1$ . Therefore, the  
 18 flame is diffusional-thermally stable, and the primary factor affecting flame  
 19 front evolution is DLI. It is seen that without DTI, the non-linear evolution of  
 20 the hydrogen/air flame exhibits a relatively simple structure at both ambient  
 21 and cryogenic temperatures. The flame propagates to the left side in a stable  
 22 single-cusp regime without cell splitting or merging processes. In addition,  
 23 the position of the single cusp on the flame front is almost the same at differ-  
 24 ent instants, i.e., the cusp stays at around  $y/\delta=7$  without lateral movement.  
 25 This indicates that DLI plays a limited role in the non-linear evolution of the

1 flame front. Combined with previous lean flame results, dynamics of non-  
 2 linear evolution, including cell splitting, cell merging, and lateral movement,  
 3 are more associated with the DTI.

4 Nevertheless, the intensity of flame instability is different for  $T_0 = 100$  K  
 5 and  $T_0 = 300$  K. Comparison between Figs. 4(a) and (b) shows that the  
 6 normalized cell depth is larger at a cryogenic temperature of  $T_0 = 100$  K.  
 7 This demonstrates that DLI is enhanced at cryogenic temperatures in the  
 8 non-linear stage.

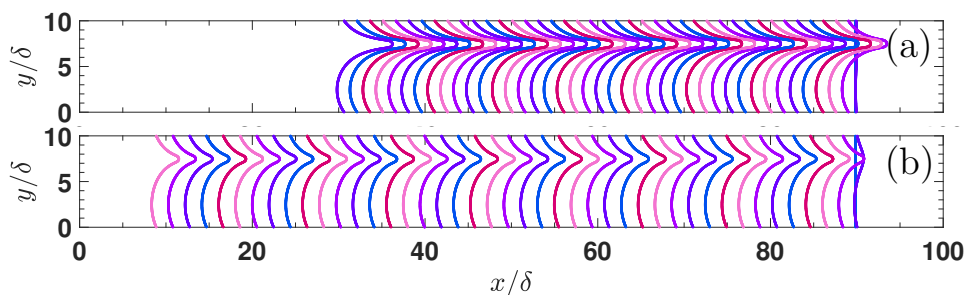


Figure 4: Temporal evolution of flame front propagating in a channel with  $h = 10\delta$  for (a)  $T_0 = 100$  K,  $\phi=1$ , (b)  $T_0 = 300$  K,  $\phi=1$ . The flame propagates from the right to the left.

9 Simulations were also performed on the fuel-rich hydrogen/air mixture  
 10 with  $\phi=2.5$ . The flame evolution in the non-linear stage is similar to the  
 11 stoichiometric case shown in Fig. 4. The results for  $\phi=2.5$  are not shown here  
 12 to avoid duplication. The primary difference between ambient and cryogenic  
 13 flames is the normalized cusp depth, which is larger for  $T_0 = 100$  K, indicating  
 14 stronger DLI at lower temperatures.

15 As mentioned above, the channel width may significantly affect the flame  
 16 evolution. To study this effect, Fig. 5 shows the fuel-lean cryogenic flame  
 17 ( $T_0 = 100$  K,  $\phi=0.5$ ) propagation in channels with different widths. Note  
 18 that the evolution of the flame front for  $h = 10\delta$  is shown in Fig. 3 and is  
 19 not repeated in Fig. 5 to avoid redundancy. As the channel width increases  
 20 from  $h = 4\delta$  to  $h = 10\delta$ , the non-linear evolution of the flame front exhibits  
 21 distinguishing regimes: For  $h = 4\delta$ , the regime is a stable single-cusp flame  
 22 front, with one small cusp located at around  $y/\delta=3$ . For  $h = 5\delta$ , the flame  
 23 front is a single-cusp regime with lateral movement. When the channel width  
 24 increases to  $h = 6\delta$ , the flame regime changes again: the flame propagates  
 25 towards the unburned gas in a complex regime, in which single-cusp and two-  
 26 cusp alternately appear on the flame front. By further increasing to  $h = 8\delta$ ,

1 the flame regime is a stable double-cusp regime in which two cusps on the  
 2 flame front with a fixed position at  $y/\delta=2$  and  $y/\delta=6$ . Interestingly, the flame  
 3 front shape for  $h = 8\delta$  seems to be mirrored from that for  $h = 4\delta$ . The quasi-  
 4 steady propagation regime (stable single-cusp and double-cusp) observed in  
 5 cases with  $h = 4\delta$  and  $8\delta$  may be related to the critical wavenumber ( $k_m$ )  
 6 associated with the maximum normalized growth rate. According to the  
 7 results in Fig. 2,  $k_m \approx 1.32$ , corresponding to a critical wavelength of  $\lambda_m \approx$   
 8  $4.7\delta$ . The channel widths for the quasi-steady propagation regime are close  
 9 to, but slightly smaller than, the integer multiples of  $\lambda_m$ . This observation is  
 10 also consistent with the results in the previous study [24]. When the channel  
 11 width is  $h = 10\delta$ , as shown in Fig. 3(a), the flame propagation regime is  
 12 alternative single-cusp and double-cusp. Therefore, the non-linear evolution  
 13 of the flame front is very sensitive to the change in channel width.

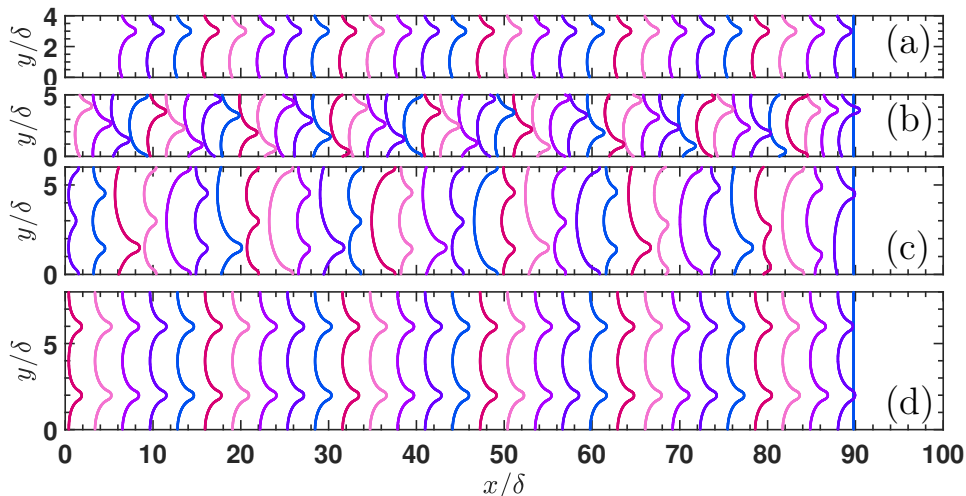


Figure 5: Temporal evolution of fuel-lean cryogenic flame ( $T_0 = 100$  K and  $\phi=0.5$ .) front propagating in channels with different widths: (a)  $h = 4\delta$ , (b)  $h = 5\delta$ , (c)  $h = 6\delta$ , and (d)  $h = 8\delta$ . The flame propagates from the right to the left.

14 Previous studies [30, 36, 48] have shown that the channel width strongly  
 15 influences the flame structure. The “flame finger” structure [36] cannot be  
 16 observed when the channel width is too small. It is found that the channel  
 17 width larger than  $25\delta$  is proper for the evolution of flame finger structure. As  
 18 shown in Fig. 6(a), one flame finger structure can be observed for  $h = 20\delta$ .  
 19 Moreover, the flame finger is smooth, and small wrinkles do not appear on the  
 20 flame branches that compose the flame finger structure. When the channel

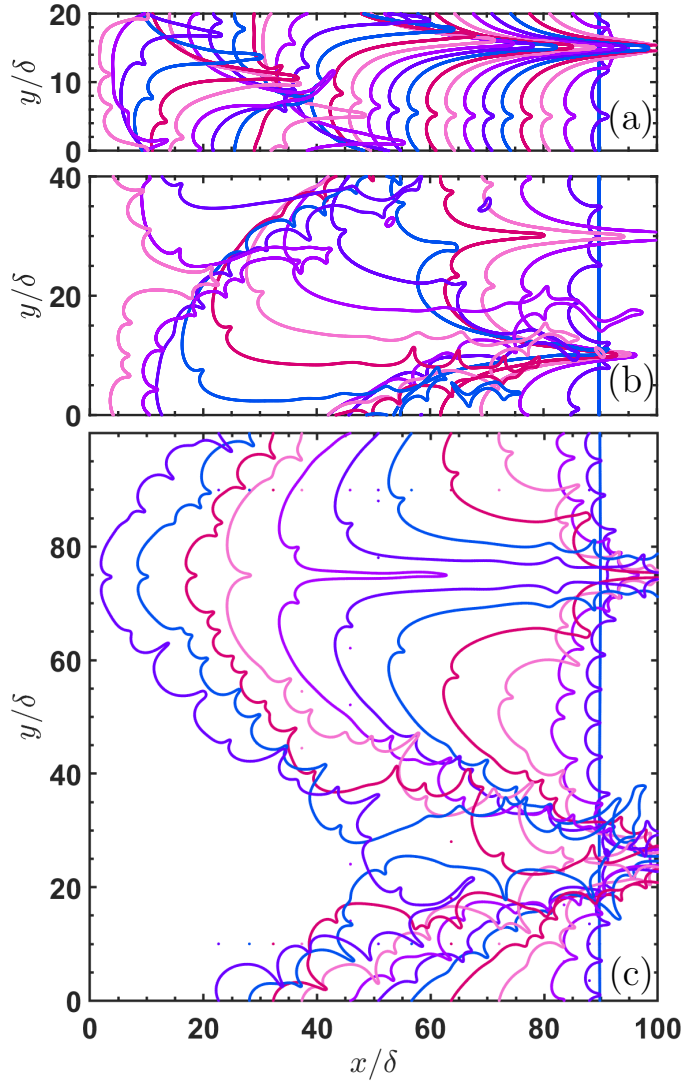


Figure 6: Temporal evolution of flame front propagating in channels with different widths (a)  $h = 20\delta$ , (b)  $h = 40\delta$ , and (c)  $h = 100\delta$  for  $T_0 = 100$  K and  $\phi=0.5$ . The flame propagates from the right to the left.

- 1 width increases to  $h = 40\delta$ , as shown in Fig. 6(b), a flame finger structure
- 2 with small wrinkles superimposed on its branches is observed. This structure
- 3 exhibits distinct lateral movement. In addition, isolated flame pockets can
- 4 be observed in the late stage due to the collision of wrinkled flame segments.
- 5 The results for  $h = 100\delta$  are shown in Fig. 6(c). After transitioning to the

1 non-linear stage, small flame finger structures with lateral movement can  
 2 merge into a large flame finger. There are many small wrinkles with different  
 3 length scales on the branches of the flame finger. The flame front is wrinkled  
 4 and accelerated as it propagates towards the unburnt gas.

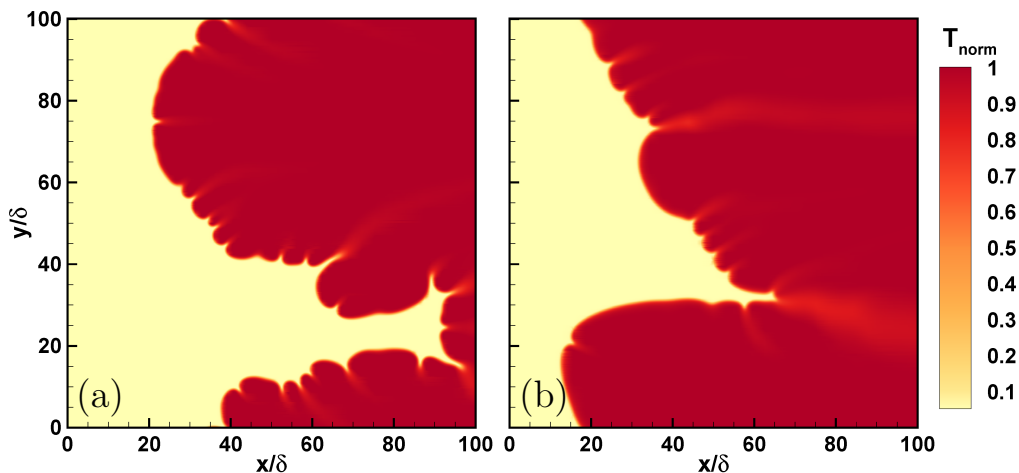


Figure 7: Contours of normalized temperature ( $T_{norm}$ ) for (a)  $T_0 = 100$  K at  $t = 20.8$  and (b)  $T_0 = 300$  K at  $t = 92$ . The channel width is  $h = 100\delta$ .

5 The contours of normalized temperature ( $T_{norm} = (T - T_0)/(T_b - T_0)$ ) at  
 6 the instant when a cellular structure is fully developed are shown in Fig. 7. It  
 7 is seen that the cryogenic flame front is more wrinkled compared to the ambi-  
 8 ent flame. In addition, the intense wrinkling of the cryogenic flame forms  
 9 a deep channel containing unburnt gas between large flame finger structures.  
 10 The subsequent combustion of the unburnt gas within the deep channel pro-  
 11 duces a sharp reduction in the flame surface area. As a result, the surface  
 12 area of the cryogenic flame can vary significantly during propagation. Con-  
 13 sistent with previous study [49], super-adiabatic temperature phenomena are  
 14 observed for both fuel-lean flames, with  $T_{norm,max} = 1.1$  for  $T_0 = 100$  K and  
 15  $T_{norm,max} = 1.05$  for  $T_0 = 300$  K. Since the super-adiabatic temperature  
 16 phenomena are associated with the imbalance between thermal and species  
 17 diffusion, the larger super-adiabatic temperature at cryogenic conditions in-  
 18 dicates that DTI is more pronounced at lower temperatures.

19 It is clear that the alternating appearance of single-cusp and double-cusp  
 20 flame fronts and the evolution of flame finger structures in fuel-lean premixed  
 21 hydrogen/air flames are closely related to long-term dynamics, including cell

1 splitting, cell merging, and lateral movement [29]. To better understand the  
2 flame evolution, their mechanisms are analyzed in the following subsection.

### 3 *3.3. Long-term flame dynamics*

4 To investigate the mechanism for cellular structure splitting and merging,  
5 the evolution of the heat release rate (HRR) contour and the corresponding  
6 flow field near the flame front is considered for the fuel-lean cryogenic case  
7 ( $T_0 = 100$  K,  $\phi=0.5$ ,  $h = 10\delta$ ). The flame front is defined as the iso-contour  
8 line of the mass fraction of  $H_2O$ , which corresponds to the maximum tempera-  
9 ture gradient of the 1D unstretched planar flame. Streamlines near the flame  
10 front are superimposed on the HRR contour to interpret the cell splitting  
11 and merging process in Figs. 8(1a-1c) and 8(2a-2c), respectively. Figure 9  
12 shows the profiles of flow speed in the  $x$  direction  $U_x$ , local heat release rate  $q$ ,  
13 density-weighted displacement speed  $S_d^*$ , stretch rate  $K$  along the flame front  
14 and the flame front position  $x$  as functions of  $y$  for several instants during  
15 the cell splitting and merging processes. It is noted that in Figs. 9(1e) and  
16 (2e) the flow direction in the unburnt region is from bottom to top and all  
17 parameters except  $q$  are normalized.

18 The splitting process of cellular structure is relevant to the interactions  
19 between the flame stretch, local reactivity, and flow. In Fig. 8(1a) at  $t=56.4$ ,  
20 the flame cell is relatively smooth, and a large cusp is located at around  
21  $y/\delta=2$ . A streamline focusing phenomenon is observed near the cusp. As  
22 shown in Fig. 9(1a), the unburnt gas speed ahead of the cusp is larger than  
23 that near the convex segment of the cell. This is a feature of DLI due to  
24 the interaction between the flame front and the flow near it [11, 20]. Gas  
25 expansion across the flame front induces flow acceleration, which enhances  
26 the flame front wrinkling and leads to a deeper cusp. In the middle of the  
27 large cell at around  $y/\delta=8$ , the flame stretch rate becomes negative, and  
28 the HRR is relatively small compared with the two flame branches near it,  
29 which can be seen in Figs. 9(1b) and (1d) at  $t=56.4$ . Therefore, a small  
30 concave segment towards the unburnt gas is formed, indicating the birth of  
31 a new cusp. As this concave segment evolves in the flow, its depth increases  
32 due to the interaction between flow and flame front, as shown in Figs. 8(1b)  
33 and 9(1a-1e). This process is relevant to the development of DLI. There-  
34 fore, the streamline focusing phenomenon becomes significant near the new  
35 cusp at around  $y/\delta=8$ . In Figs. 8(1c) and 9(1e), this new cusp forms with  
36 considerable depth. Note that the interaction between flame stretch and  
37 chemistry also plays an important role in the cell splitting process since the

1 cusp deepening process is accompanied by a change in curvature and flame  
 2 stretch rate that affects the chemical reaction through Lewis number effect,  
 3 as shown in Figs. 9(1b) and (1d). In summary, the complex interactions  
 4 between flow, flame stretch, and chemistry lead to the splitting of flame cells  
 5 and the formation of a new cusp on the flame front.

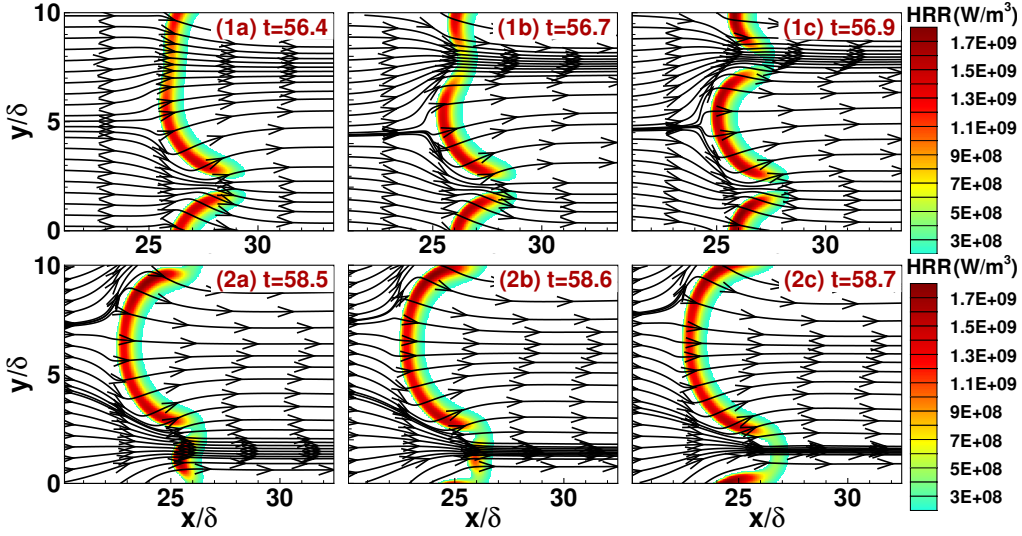


Figure 8: Evolution of heat release rate contour superimposed by streamlines near the occurrence of cell splitting (1a-1c) and cell merging event (2a-2c) for  $T_0 = 100$  K and  $\phi=0.5$ . The channel width is  $h = 10\delta$ .

6 The cell merging process is shown in Figs. 8(2a-2c) and 9(2a-2e). Note  
 7 that a periodic boundary condition is imposed in the  $y$  direction. At  $t=58.5$   
 8 in Figs. 8(2a) and 9(1e), the flame front consists of two convex cells with  
 9 different length-scales: a large cell within the range of  $2.5 \leq y/\delta \leq 10$  and  
 10 a small cell within  $0 \leq y/\delta \leq 2.5$ . These two cells are connected by two  
 11 cusps between them. Since the HRR on the larger cell is not uniform, the  
 12 propagation speed is different along the flame front of the large cell. Specif-  
 13 ically, the HRR is larger on two branches of the large cell near the cusps  
 14 and smaller in the middle of the cell. This can be observed in Figs. 8(2a-2c)  
 15 and 9(2b). Therefore, the large cell tends to expand in the lateral direction  
 16 ( $y$  direction), which narrows the channel ahead of the small cell, as shown  
 17 in Figs. 8(2b) and 9(2a-2e). Flow focusing also contributes to the increase  
 18 in cusp depth. The narrow channel ahead of the small cell acts like a ‘cusp’,  
 19 and therefore, the flow speed in the ‘cusp’ ( $0 \leq y/\delta \leq 2.5$ ) increases as the

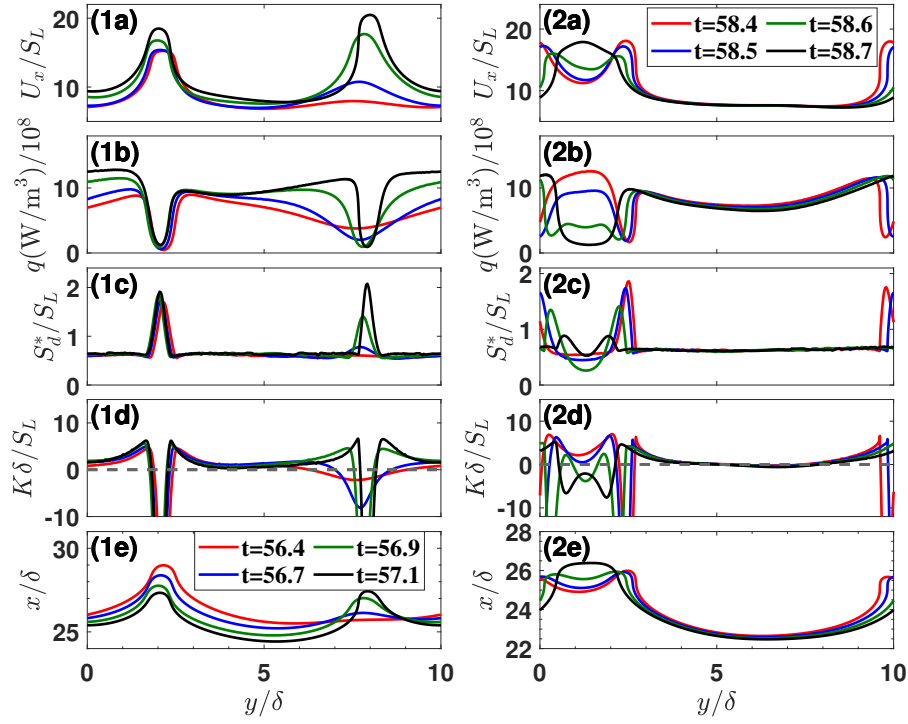


Figure 9: Temporal evolution of profiles for flow speed,  $U_x$ , heat release rate,  $q$ , density-weighted displacement speed,  $S_d^*$ , stretch rate,  $K$ , and the flame front position,  $x$ , along the flame front during cell splitting (1a-1e) and cell merging process (2a-2e).

1 large cell expands, as shown in Figs. 8(2b) and 9(2a). Due to the increased  
2 flow speed, the small flame cell cannot propagate towards the unburnt gas  
3 on the left. Gradually, it is pushed back by the strong flow. As a result, the  
4 small cell becomes flat (see Fig. 9(2e)). Since the differential diffusion effect  
5 is strong for this negatively stretched flame segment (see in Fig. 9(2d)), the  
6 HRR of the smaller cell also decreases gradually during this process, which  
7 can be seen in Fig. 9(2b). Finally, as shown in Fig. 8(2c), the small cell  
8 disappears, implying the completion of the cell merging process. Therefore,  
9 the cell merging is also associated with the interaction between flow, flame  
10 stretch, and chemical reactions.

11 In addition, Fig. 9(1b) also explains the mechanism for the lateral move-  
12 ment of cusps. At  $t=56.9$  (green line), there is a manifest difference in heat  
13 release rate between the two flame branches forming the cusp at  $y/\delta=2$ . Af-  
14 fected by this, the flame propagation speeds are also different. Therefore, the

1 strong flame branch near  $y/\delta=1$  pushes the weak flame branch near  $y/\delta=3$ ,  
 2 leading to the lateral movement of the cusp towards the  $y$ -axis direction.  
 3 Therefore, the cusp moves to the right from  $t=56.9$  to  $t=57.1$  (black line),  
 4 which can be seen from Fig. 9(1e). As mentioned above, the HRR distri-  
 5 bution is affected by the cell splitting and merging processes. Therefore,  
 6 lateral movement is frequently observed for flames in the regime of alter-  
 7 native appearance of single-cusp and double-cusp, as can be observed in  
 8 Figs. 3, 5(b), 5(c) and 6.

9 In summary, strong interaction among flow, flame stretch, and chemical  
 10 reactions (heat release) plays a primary role in the cell splitting and merging  
 11 processes. Therefore, the mechanisms of the chaotic evolution of the fuel-lean  
 12 flame front are relevant to the ‘flow-stretch-chemistry’ interaction.

### 13 3.4. Cellular flame structure

14 In order to interpret the effect of cryogenic temperatures on the local flame  
 15 structure, the joint distribution of progress variable (PV) and the normalized  
 16 reaction rate of hydrogen are analyzed. The progress variable is defined as

$$PV(Y(\text{H}_2)) = 1 - \frac{Y(\text{H}_2) - Y_b(\text{H}_2)}{Y_u(\text{H}_2) - Y_b(\text{H}_2)} \quad (5)$$

17 where  $Y(\text{H}_2)$  is the mass fraction of  $\text{H}_2$ ,  $Y_u(\text{H}_2)$  and  $Y_b(\text{H}_2)$  are the mass  
 18 fraction of  $\text{H}_2$  in the unburnt and burned gas, respectively.

19 The joint distribution, conditional average and 1D unstretched planar  
 20 flame solution of progress variable and corresponding source term for case  
 21  $h = 10\delta$  are shown in Fig. 10. It is seen that for the fuel-lean flames, the  
 22 conditional average of source term is much higher than the 1D unstretched  
 23 flame solution. On the other hand, in Fig. 10(c), the cryogenic flame at  $\phi=1$ ,  
 24 the conditional average of source term is close to the 1D unstretched planar  
 25 flame solution, indicating that the effects of DLI on local flame structure  
 26 and the enhancement in reaction rate are negligible. Comparison in Fig. 10  
 27 demonstrates that DTI of fuel-lean flames has a significant impact on the lo-  
 28 cal reaction rate enhancement. Therefore, DLI accelerates flame propagation  
 29 mainly through the increase in the flame surface area, while DTI can lead to  
 30 flame acceleration through both an increase in the flame surface area and lo-  
 31 cal reaction rate enhancement. Furthermore, compared to the ambient flame  
 32 at  $T_0 = 300$  K and  $\phi=0.5$ , the cryogenic flame at  $\phi=0.5$  exhibits a larger  
 33 normalized conditional average of the source term, which demonstrates that

1 at a lower temperature, the DTI has a stronger influence on local reaction  
 2 rate enhancement.

3 To assess the effect of channel width on flame propagation, the joint  
 4 distribution of the progress variable and the corresponding source term for  
 5  $h = 100\delta$  is shown in Fig. 11. It is seen that the normalized conditional  
 6 averages of the source term do not change significantly from cases  $h = 10\delta$   
 7 shown in Fig. 10. Therefore, increasing the channel width from  $h = 10\delta$  to  
 8  $h = 100\delta$  has a limited effect on the local reaction rate enhancement for the  
 9 fuel-lean flames considered in this work.

### 10 3.5. Flame acceleration

11 Strong DLI and DTI can greatly enhance the flame front wrinkling, ac-  
 12 celerating flame propagation. An approximate measure of the flame speed  
 13 for the wrinkled flame is consumption speed,  $S_c$ , defined as in [31],

$$S_c = \frac{1}{\rho_u(Y_u(\text{H}_2) - Y(\text{H}_2)) \cdot A_0} \int \dot{\omega} dx dy \quad (6)$$

14 where  $\dot{\omega}$  is the net consumption rate of  $\text{H}_2$ ,  $\rho_u$  the unburned gas density,  
 15  $Y_u(\text{H}_2)$  the mass fraction of  $\text{H}_2$  in the unburned gas,  $A_0$  the flame surface  
 16 area at  $t=0$ , i.e.,  $A_0 = h$ . Generally, flame instabilities can affect overall  
 17 flame speed through two mechanisms: flame surface area increase due to  
 18 flame wrinkling and local flame speed change related to flame stretch [36, 50].  
 19 To quantify their individual effect,  $S_c$  is decomposed into the production of  
 20 flame surface area increase  $A/A_0$  and stretch factor  $I$ ,

$$S_c/S_L = I \cdot (A/A_0) \quad (7)$$

21 where  $A$  is the surface area of the wrinkled flame front. It is noted that the  
 22 fuel-lean flame surface is defined as the iso-contour line of  $PV(Y(\text{H}_2))=0.9$  [49].  
 23 This definition leads to reasonable results for the flame surface area, espe-  
 24 cially for the fuel-lean flame, which is prone to strong DTI. For stoichiometric  
 25 or fuel-rich cases, the iso-contour line of water mass fraction ( $Y(\text{H}_2\text{O})$ ) corre-  
 26 sponding to the maximum temperature gradient of the 1D unstretched planar  
 27 flame is selected to the calculated flame surface area, as the differential dif-  
 28 fusion effect could lead to locally fuel-rich mixture [31]. The stretch factor  
 29 measures the effect of local reactivity on the consumption speed. If  $I > 1$ ,  
 30 the effect of flame stretch enhances the consumption of fuel (local reaction  
 31 rates) and vice versa.

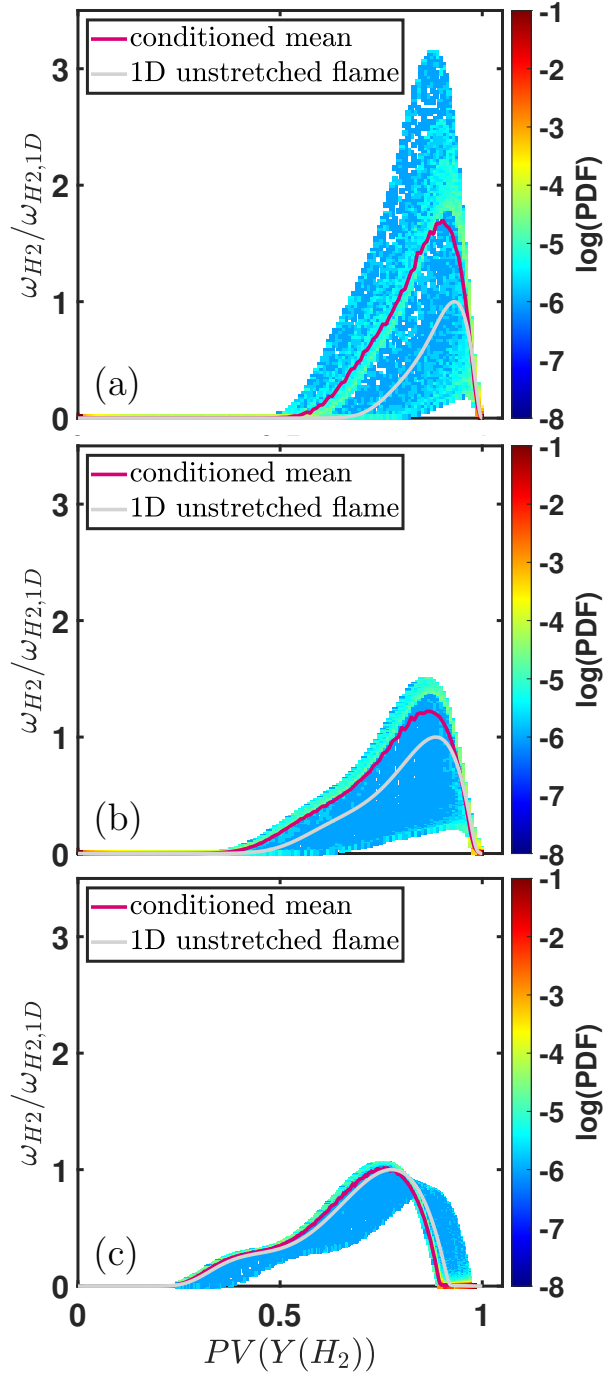


Figure 10: Joint distribution, conditional average (red line) and 1D unstretched flame solution (grey line) of the progress variable  $PV(Y(H_2))$  and the normalized source term of  $PV(Y(H_2))$  for (a)  $T_0 = 100$  K,  $\phi=0.5$ , (b)  $T_0 = 300$  K,  $\phi=0.5$ , and (c)  $T_0 = 100$  K,  $\phi=1$ . The channel width is  $h = 10\delta$ .

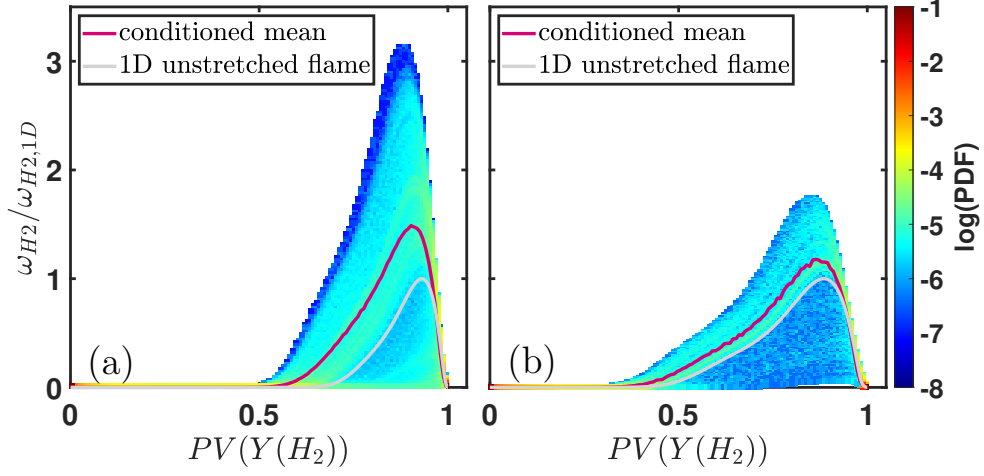


Figure 11: Joint distribution, conditional average (red line) and 1D unstretched flame solution (grey line) of the progress variable  $PV(Y(H_2))$  and the normalized source term of  $PV(Y(H_2))$  for (a)  $T_0 = 100$  K,  $\phi=0.5$  and (b)  $T_0 = 300$  K,  $\phi=0.5$ . The channel width is  $h = 100\delta$ .

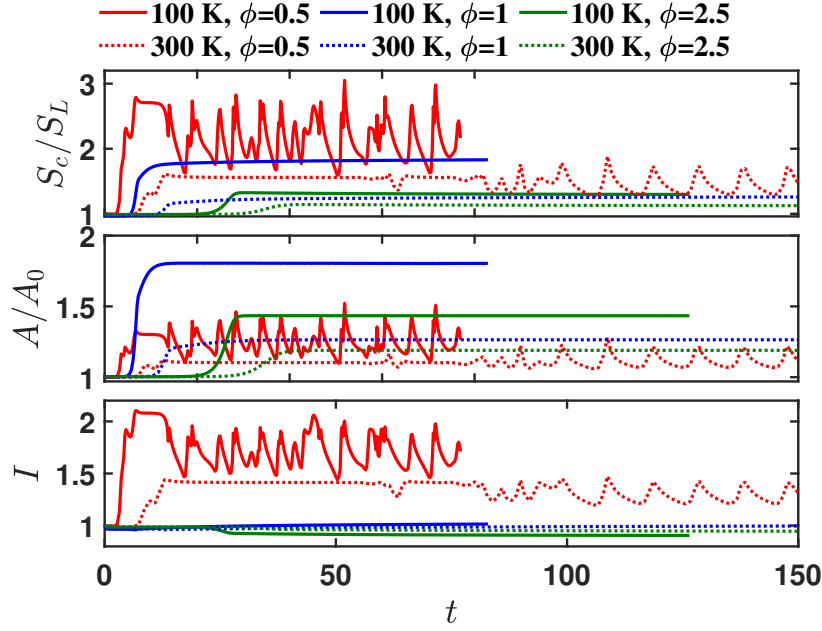


Figure 12: Evolution of the normalized consumption speed  $S_c/S_L$ , flame surface area increase  $A/A_0$  and stretch factor  $I$  for case  $T_0 = 100$  K and  $\phi=0.5$ ,  $h = 100\delta$ .

1 The effect of equivalence ratio and cryogenic temperatures on flame evo-  
 2 lution for  $h = 10\delta$  is shown in Fig.12. It is found that the consumption speed  
 3 oscillation is only observed for  $\phi = 0.5$  with strong DTI. This result is rea-  
 4 sonable since the chaotic evolution of cellular structure originates from DTI.  
 5 On the other hand, the acceleration of fuel-lean cryogenic flame is the most  
 6 pronounced, highlighting that the combined effects of both DLI and DTI  
 7 have a significant influence on flame acceleration. Further analyses shown in  
 8 Figs. 12(b) and (c) demonstrate that the acceleration results from enhance-  
 9 ment in both  $A/A_0$  and  $I$ . The primary contribution is from the increase in  
 10  $I$ . This shows that DTI is the dominant factor in fuel-lean flame acceleration,  
 11 consistent with the previous study [36]. In addition, pure DLI also leads to  
 12 intense flame acceleration, which can be seen in the cryogenic and ambient  
 13 cases at  $\phi = 1$ . For fuel-rich flames, flame acceleration is greatly suppressed,  
 14 with  $S_c/S_L$  close to 1. It is clear that for  $\phi \geq 1$ , the acceleration is purely  
 15 caused by an increase in  $A/A_0$ . The local reaction rate is not enhanced by  
 16 DLI, which is consistent with the results shown in Fig. 10(c).

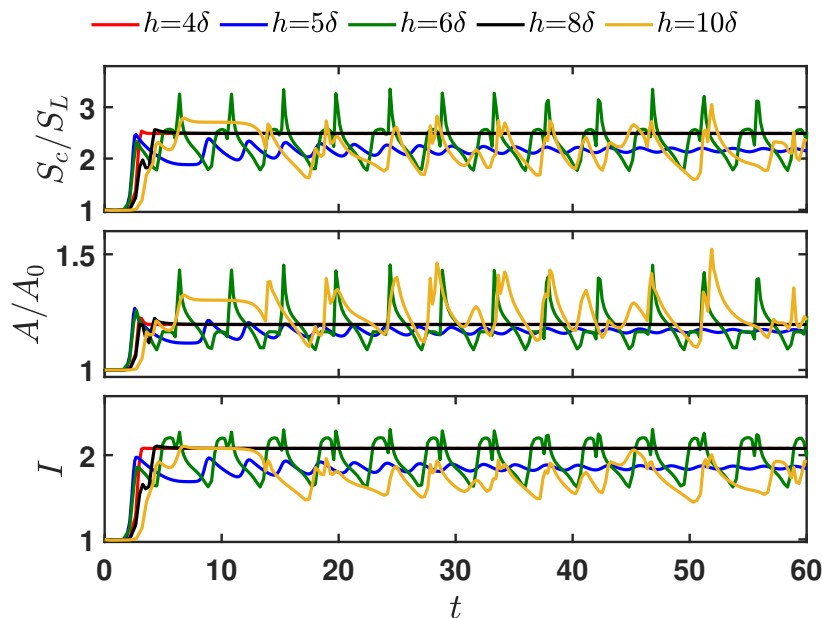


Figure 13: Evolution of the normalized consumption speed  $S_c/S_L$ , flame surface area increase  $A/A_0$  and stretch factor  $I$  for case  $T_0 = 100$  K and  $\phi=0.5$  in domain with different widths  $h$ .

17 Figure 13 shows the effect of channel width ( $h \leq 10\delta$ ) on the flame

1 acceleration in the fuel-lean mixture at  $T_0 = 100$  K. The flame speed changes  
 2 periodically due to chaotic cell evolution. The time period of oscillations is  
 3 affected by both the channel width and the lateral movement speed. However,  
 4 the lateral movement speed is complex and can be affected by many factors,  
 5 such as the nonlinear behavior of the flame front, the Lewis number and the  
 6 temperature distribution along the flame front [51]. Deriving an analytical  
 7 expression for the oscillation period is beyond the scope of this work and  
 8 warrants further investigation. In addition, the flame speed enhancement,  
 9  $S_c/S_L$ , is larger than 1.5 for all channel widths considered. Both  $A/A_0$  and  $I$   
 10 contribute to the flame acceleration. Moreover, Fig. 13 shows that the stretch  
 11 factor  $I$  oscillates around  $I = 2.0$  with a lower bound of  $I > 1.5$ , while  $A/A_0$   
 12 fluctuates around  $A/A_0 = 1.2$  with an upper bound of  $A/A_0 < 1.5$ . Since  $I$   
 13 is only relevant to the DTI and the DTI also contributes to  $A/A_0$ , it can be  
 14 concluded that the DTI plays a dominant role in fuel-lean flame propagation.  
 15 Previous studies [36, 50] have shown that DLI can enhance the development  
 16 of DTI. Therefore, DLI may also play a role in flame acceleration through  
 17 a direct mechanism of increasing flame surface area or through an indirect  
 18 mechanism of promoting DTI. It is worth noting that the dependence of  
 19  $S_c/S_L$ ,  $A/A_0$  and  $I$  on  $h$  is sensitive, which is caused by the chaotic evolution  
 20 of the flame front under strong DTI and DLI. Therefore, channel width has a  
 21 significant effect on flame evolution regimes and thereby flame acceleration,  
 22 especially for narrow channels.

Table 3: The mean values of normalized consumption speed  $S_c/S_L$ , flame surface area  
 increase  $A/A_0$ , and stretch factor  $I$  for fuel-lean hydrogen/air flame at  $T_0 = 100$  K and  
 300 K. The channel width is  $h = 100\delta$ .

case	$S_c/S_L$	$A/A_0$	$I$
$T_0 = 100$ K	4.25	1.95	2.17
$T_0 = 300$ K	2.04	1.40	1.45

23 As mentioned above, a large domain is necessary to obtain geometry-  
 24 independent results. For flame propagation in wide channels, the results are  
 25 shown in Fig. 14. Based on the data after the cellular structure is fully devel-  
 26 oped in the wide channel of  $h = 100\delta$ , the domain-independent mean values  
 27 of  $S_c/S_L$ ,  $A/A_0$ , and  $I$  for fuel-lean hydrogen/air flames at  $T_0 = 100$  K and  
 28 300 K are calculated and listed in Table 3. Compared to  $T_0 = 300$  K, the  
 29 larger  $S_c/S_L$  at  $T_0 = 100$  K results from the increase in both  $A/A_0$  and  $I$ ,

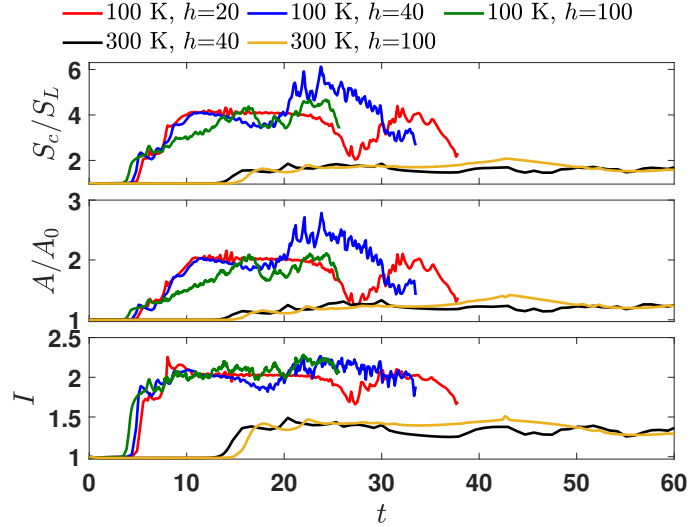


Figure 14: Evolution of the normalized consumption speed  $S_c/S_L$ , flame surface area increase  $A/A_0$  and stretch factor  $I$  for  $\phi=0.5$  in domain with different widths and initial temperatures.

1 which demonstrates that both DLI and DTI are enhanced under cryogenic  
 2 conditions. Since the values of  $I$  are larger than  $A/A_0$ , the DTI has a greater  
 3 contribution to the flame acceleration than the DLI. It is noted that the mean  
 4 values in Table 3 for the cryogenic flame are calculated during the later stage  
 5 of flame propagation, when most of the flame segments are contained within  
 6 the computational domain. A small portion of flame segments extending be-  
 7 yond the domain may lead to slightly underestimated mean values; however,  
 8 this does not affect the main conclusions.

9 Comparison between Figs. 13 and 14 shows that the periodic oscillation  
 10 phenomena disappear when the channel width is large. Only small spikes  
 11 appear on the evolution of consumption speed in Fig. 14. This is reasonable  
 12 since the cellular flame front evolution is more violent without the confine-  
 13 ment of channel width. Additionally, the large oscillations observed in Fig.  
 14 14 are relevant to the flame segments extending beyond the computational  
 15 domain, which causes a pronounced reduction in flame surface area and flame  
 16 consumption speed. Compared to small channels shown in Fig. 13, the value  
 17 of  $A/A_0$  for a cryogenic flame increases to around  $A/A_0 \approx 1.95$ , while the  
 18 stretch factor  $I$  does not increase significantly. Therefore, a small channel  
 19 width can suppress the development of flame instabilities through the flame

1 surface area, resulting in weaker flame acceleration. On the other hand, the  
2 stretch factor  $I$  is less sensitive to the channel width, which agrees well with  
3 the analysis in the previous section.

4 An interesting observation is the large value of  $S_c/S_L \approx 6$  for  $h = 40\delta$   
5 in Fig. 14(a) and 14(b) shows that this large value is associated with an  
6 increase in flame surface area, resulting from the formation of a very deep  
7 cusp during the flame propagation, as shown in Fig. 6(b). Compared to the  
8 case with  $h = 100\delta$ , a smaller channel width of  $h = 40\delta$  enhances the flame  
9 acceleration. Therefore, a smaller channel width does not always suppress  
10 the flame wrinkling and flame acceleration. This also indicates that channel  
11 width has a great impact on cellular flame evolution and acceleration.

## 12 4. Conclusions

13 The evolution and acceleration of fuel-lean hydrogen/air flames at ambi-  
14 ent and cryogenic temperatures (300 K and 100 K) are studied by a series  
15 of two-dimensional simulations incorporating detailed chemistry and trans-  
16 port models. The analysis reveals that cryogenic temperatures significantly  
17 enhance both Darrieus-Landau instability (DLI) and diffusional-thermal in-  
18 stability (DTI) of fuel-lean hydrogen/air flames. In the linear stage, the  
19 growth rates of both DLI and DTI are found to increase significantly at  
20 cryogenic temperatures. The non-linear stage of cellular flame evolution ex-  
21 hibits chaotic characteristics influenced by unburned gas temperature and  
22 channel width, with DTI emerging as the primary driver of this chaotic evolu-  
23 tion. Long-term dynamics of cellular structures, including cell splitting, cell  
24 merging, and lateral movement, are observed and interpreted for fuel-lean  
25 hydrogen/air flames. It is found that cell splitting and merging are mainly  
26 caused by the flow-stretch-chemistry interaction. The unbalanced heat re-  
27 lease rate on two branches of the cusp can induce the lateral movement of  
28 cusps. In the absence of DTI, the flame propagates in a single-cusp regime  
29 without cell splitting, merging, or lateral movement due to a relatively weak  
30 stretch-chemistry interaction.

31 Flame structure analysis reveals a significant enhancement of local re-  
32 action rates in lean hydrogen/air flames under cryogenic conditions. For  
33 diffusive-thermally stable hydrogen/air flames with  $\phi = 1$ , the cryogenic tem-  
34 perature has a negligible effect on the local reaction rate. The pronounced  
35 acceleration of fuel-lean cryogenic flames stems from the simultaneous en-  
36 hancement of flame surface area and stretch factor, reflecting the combined

1 influence of DLI and DTI. While both instabilities contribute to flame ac-  
2 celeration, DTI emerges as the dominant mechanism, with DLI providing  
3 secondary enhancement. The flame evolution demonstrates particular sensi-  
4 tivity to channel geometry when the width  $h < 10\delta$ : minor width variations  
5 can substantially alter the evolution of flame consumption speed. Further  
6 analysis indicates that channel width influences flame behavior primarily by  
7 constraining the flame surface area, while local reaction rates remain largely  
8 independent of geometric constraints.

9 In this study, the Soret diffusion is not considered. In previous study [52],  
10 the Soret diffusion effect was examined at elevated temperatures. It would  
11 be interesting to quantify the influence of the Soret diffusion at cryogenic  
12 temperatures in future studies. Our study employs two-dimensional simula-  
13 tions, which capture important aspects of flame dynamics but have inherent  
14 limitations. In real-world applications, flames propagate three-dimensionally,  
15 potentially exhibiting additional instability mechanisms that could enhance  
16 flame front wrinkling and acceleration beyond what we observe in two di-  
17 mensions. Introducing the third dimension may reveal new patterns of flame  
18 evolution and more complex interactions between DLI and DTI. Future in-  
19 vestigations using three-dimensional simulations in large computational do-  
20 mains would complement our current findings and provide a more complete  
21 understanding of flame behavior under cryogenic conditions.

## 22 **5. Declaration of competing interest**

23 The authors declare that they have no known competing financial inter-  
24 ests or personal relationships that could have appeared to influence the work  
25 reported in this paper.

## 26 **6. Acknowledgments**

27 This work was funded by the National Natural Science Foundation of  
28 China (No. 52425604). This work was supported by funding from the  
29 Engineering and Physical Sciences Research Council IAA (Grant number  
30 EP/R511742/1). Dr. Linlin Yang gratefully acknowledges the financial sup-  
31 port from the John Fell Oxford University Press Research Fund (0016719).  
32 Dr. Fang acknowledges the financial support provided by the NSERC and  
33 Alberta Innovate HCOE2 program. We also thank Dr. Hannes Böttler at  
34 the Technical University of Darmstadt for helpful discussions.

1 **References**

- 2 [1] Z. Abdin, A. Zafaranloo, A. Rafiee, W. Mérida, W. Lipiński, K. R.  
3 Khalilpour, Hydrogen as an energy vector, *Renew. Sustain. Energy Rev.*  
4 120 (2020) 109620.
- 5 [2] T. Lehmann, L. Berger, T. L. Howarth, M. Gauding, S. Girhe, B. B.  
6 Dally, H. Pitsch, Comprehensive linear stability analysis for intrinsic in-  
7 stabilities in premixed ammonia/hydrogen/air flames, *Combust. Flame*  
8 273 (2025) 113927.
- 9 [3] M. Aziz, Liquid Hydrogen: A Review on Liquefaction, Storage, Trans-  
10 portation, and Safety, *Energies* 14 (2021) 5917.
- 11 [4] G. Tretola, L. Shen, F. Leach, K. Vogiatzaki, Mixing and Warming  
12 Characterisation of Cryogenic Hydrogen Jets Through Proper Orthogo-  
13 nal Decomposition, in: *ASME 2024 ICE Forward Conference*, American  
14 Society of Mechanical Engineers, San Antonio, Texas, USA, 2024, p.  
15 V001T06A012.
- 16 [5] D. Yu, Z. Chen, Premixed flame ignition: Theoretical development,  
17 *Prog. Energy Combust. Sci.* 104 (2024) 101174.
- 18 [6] S. Lai, S. Tang, C. Xu, N. Sekularac, X. Fang, Computational diagnos-  
19 tics for flame acceleration and transition to detonation in a hydrogen/air  
20 mixture, *Combust. Flame* 258 (2023) 113054.
- 21 [7] M. Kuznetsov, A. Denkevits, A. Vesper, A. Friedrich, Flame propagation  
22 regimes and critical conditions for flame acceleration and detonation  
23 transition for hydrogen-air mixtures at cryogenic temperatures, *Int. J.*  
24 *Hydrog. Energy* 47 (2022) 30743–30756.
- 25 [8] J. X. Wen, E. S. Hecht, R. Mevel, Recent advances in combustion sci-  
26 ence related to hydrogen safety, *Prog. Energy Combust. Sci.* 107 (2025)  
27 101202.
- 28 [9] Y. Wang, X. Guan, S. Xie, M. Zhou, Z. Zhang, Z. Chen, T. Zhang,  
29 Numerical studies on the ignition and propagation for spherically ex-  
30 panding premixed cool flames under gravitational conditions, *Combust.*  
31 *Flame* 259 (2024) 113194.

- 1 [10] C. K. Law, *Combustion Physics*, Cambridge University Press, Cam-  
2 bridge, 2006.
- 3 [11] M. A. Liberman, *Combustion Physics: Flames, Detonations, Ex-*  
4 *plosions, Astrophysical Combustion and Inertial Confinement Fusion*,  
5 Springer International Publishing, Cham, 2021.
- 6 [12] P. Clavin, G. Searby, *Combustion Waves and Fronts in Flows: Flames,*  
7 *Shocks, Detonations, Ablation Fronts and Explosion of Stars*, Cam-  
8 bridge University Press, Cambridge, United Kingdom, 2016.
- 9 [13] M. Matalon, The Darrieus–Landau instability of premixed flames, *Fluid*  
10 *Dyn. Res.* 50 (2018) 051412.
- 11 [14] L. Yang, Y. Wang, Z. Chen, Propagation and self-acceleration of circu-  
12 lar expanding hydrogen/air flames at cryogenic temperature, *Combust.*  
13 *Flame* 265 (2024) 113501.
- 14 [15] L. Berger, A. Attili, H. Pitsch, Intrinsic instabilities in premixed hy-  
15 drogen flames: Parametric variation of pressure, equivalence ratio, and  
16 temperature. Part 1 - Dispersion relations in the linear regime, *Combust.*  
17 *Flame* 240 (2022) 111935.
- 18 [16] L. Yang, Z. Chen, Effects of cryogenic temperature on premixed hydro-  
19 gen/air flame propagation in a closed channel, *Proc. Combust. Inst.* 39  
20 (2023) 2991–2999.
- 21 [17] L. Yang, Y. Wang, T. Zirwes, F. Zhang, H. Bockhorn, Z. Chen, Ef-  
22 fects of Intrinsic Instabilities on the Response of Premixed Hydrogen/Air  
23 Conical Flames to Inlet Flow Perturbations, *Flow Turbulence Combust*  
24 112 (4) (2024) 1275–1297.
- 25 [18] C. Chen, C. Chi, D. Thévenin, W. Han, L. Yang, Effects of cryogenic  
26 temperature on turbulent premixed hydrogen/air flames, *Proc. Com-*  
27 *bust. Inst.* 40 (2024) 105749.
- 28 [19] S. Missey, O. Dounia, L. Selle, Early-stage flame acceleration in stratified  
29 hydrogen-air mixtures: Theory and simulation, *Proc. Combust. Inst.* 40  
30 (2024) 105279.

- 1 [20] M. Matalon, C. Cui, J. K. Bechtold, Hydrodynamic theory of premixed  
2 flames: effects of stoichiometry, variable transport coefficients and arbitrary  
3 reaction orders, *J. Fluid Mech.* 487 (2003) 179–210.
- 4 [21] T. Zhang, Y. Ju, Structures and propagation speeds of autoignition-  
5 assisted premixed n-heptane/air cool and warm flames at elevated temperatures  
6 and pressures, *Combust. Flame* 211 (2020) 8–17.
- 7 [22] S. Mohan, M. Matalon, Numerical methodology for spontaneous wrinkling  
8 of centrally ignited premixed flames – linear theory, *Combust. Theory Model.* 25  
9 (2021) 940–967.
- 10 [23] R. Addabbo, J. Bechtold, M. Matalon, Wrinkling of spherically expanding  
11 flames, *Proc. Combust. Inst.* 29 (2002) 1527–1535.
- 12 [24] C. E. Frouzakis, N. Fogla, A. G. Tomboulides, C. Altantzis, M. Matalon,  
13 Numerical study of unstable hydrogen/air flames: Shape and propagation  
14 speed, *Proc. Combust. Inst.* 35 (2015) 1087–1095.
- 15 [25] G. Sivashinsky, Nonlinear analysis of hydrodynamic instability in laminar  
16 flames—I. Derivation of basic equations, *Acta Astronaut.* 4 (1977)  
17 1177–1206.
- 18 [26] D. Michelson, G. Sivashinsky, Nonlinear analysis of hydrodynamic instability  
19 in laminar flames—II. Numerical experiments, *Acta Astronaut.* 4  
20 (1977) 1207–1221.
- 21 [27] Y. Rastigejev, M. Matalon, Nonlinear evolution of hydrodynamically  
22 unstable premixed flames, *J. Fluid Mech.* 554 (2006) 371.
- 23 [28] Y. Rastigejev, M. Matalon, Numerical simulation of flames as gas-  
24 dynamic discontinuities, *Proc. Combust. Inst.* 10 (2006) 459–481.
- 25 [29] C. Altantzis, C. E. Frouzakis, A. G. Tomboulides, M. Matalon,  
26 K. Boulouchos, Hydrodynamic and thermodiffusive instability effects  
27 on the evolution of laminar planar lean premixed hydrogen flames, *J.*  
28 *Fluid Mech.* 700 (2012) 329–361.
- 29 [30] L. Berger, K. Kleinheinz, A. Attili, H. Pitsch, Characteristic patterns of  
30 thermodiffusively unstable premixed lean hydrogen flames, *Proc. Combust.*  
31 *Inst.* 37 (2019) 1879–1886.

- 1 [31] L. Berger, A. Attili, H. Pitsch, Intrinsic instabilities in premixed hydro-  
2 gen flames: parametric variation of pressure, equivalence ratio, and  
3 temperature. Part 2 – Non-linear regime and flame speed enhancement,  
4 *Combust. Flame* 240 (2022) 111936.
- 5 [32] E. Hunt, A. Aspden, Thermodynamically-unstable lean premixed hydro-  
6 gen flames: Length scale effects and turbulent burning regimes, *Combust.*  
7 *Flame* 272 (2025) 113855.
- 8 [33] X. Wen, L. Berger, A. Scholtissek, A. Parente, C. Hasse, H. Pitsch, Nu-  
9 merical analysis and flamelet modeling of NO<sub>x</sub> formation in a thermody-  
10 namic unstable premixed hydrogen flame at elevated-pressure condi-  
11 tions, *Proc. Combust. Inst.* 40 (2024) 105411.
- 12 [34] S. Xie, X. Chen, Y. Wang, T. Zhang, Z. Chen, Numerical study on forced  
13 ignition and flame propagation in a counterflow of nitrogen-diluted hy-  
14 drogen versus air, *Fuel* 357 (2024) 129863.
- 15 [35] A. Attili, R. Lamioni, L. Berger, K. Kleinheinz, P. E. Lapenna,  
16 H. Pitsch, F. Creta, The effect of pressure on the hydrodynamic stability  
17 limit of premixed flames, *Proc. Combust. Inst.* 38 (2021) 1973–1981.
- 18 [36] L. Berger, M. Grinberg, B. Jürgens, P. E. Lapenna, F. Creta, A. Attili,  
19 H. Pitsch, Flame fingers and interactions of hydrodynamic and thermody-  
20 namic instabilities in laminar lean hydrogen flames, *Proc. Combust.*  
21 *Inst.* 39 (2023) 1525–1534.
- 22 [37] D. G. Goodwin, R. L. Speth, H. K. Moffat, B. W. Weber, Cantera: An  
23 Object-oriented Software Toolkit for Chemical Kinetics, Thermodynam-  
24 ics, and Transport Processes (Aug. 2018).
- 25 [38] A. Nonaka, J. B. Bell, M. S. Day, C. Gilet, A. S. Almgren, M. L. Minion,  
26 A deferred correction coupling strategy for low Mach number flow with  
27 complex chemistry, *Combust. Theory Model.* 16 (2012) 1053–1088.
- 28 [39] A. A. Konnov, Yet another kinetic mechanism for hydrogen combustion,  
29 *Combust. Flame* 203 (2019) 14–22.
- 30 [40] A. Ghosh, N. M. Munoz-Munoz, K. P. Chatelain, D. A. Lacoste, Lam-  
31 inar burning velocity of hydrogen, methane, ethane, ethylene, and

- 1 propane flames at near-cryogenic temperatures, *Appl. Energy Combust.*  
2 *Sci.* 12 (2022) 100094.
- 3 [41] A. Aspden, M. Day, J. Bell, Lewis number effects in distributed flames,  
4 *Proc. Combust. Inst.* 33 (1) (2011) 1473–1480.
- 5 [42] J. F. Grcar, J. B. Bell, M. S. Day, The solet effect in naturally propagat-  
6 ing, premixed, lean, hydrogen–air flames, *Proc. Combust. Inst.* 32 (1)  
7 (2009) 1173–1180.
- 8 [43] W. Liang, C. K. Law, Z. Chen, Ignition of hydrogen/air mixtures by  
9 a heated kernel: Role of solet diffusion, *Combust. Flame* 197 (2018)  
10 416–422.
- 11 [44] S. L. Michaux, K. P. Chatelain, W. L. Roberts, D. A. Lacoste, Laminar  
12 burning velocities of hydrogen-air and methane-air flames from ambient  
13 to cryogenic temperatures at different equivalence ratios, *Int. J. Hydrog.*  
14 *Energy* 100 (2025) 608–616.
- 15 [45] D. Fernández-Galisteo, V. N. Kurdyumov, P. D. Ronney, Analysis of  
16 premixed flame propagation between two closely-spaced parallel plates,  
17 *Combust. Flame* 190 (2018) 133–145.
- 18 [46] J. Gaucherand, D. Laera, C. Schulze-Netzer, T. Poinsot, Intrinsic insta-  
19 bilities of hydrogen and hydrogen/ammonia premixed flames: Influence  
20 of equivalence ratio, fuel composition and pressure, *Combust. Flame* 256  
21 (2023) 112986.
- 22 [47] J. Yuan, Y. Ju, C. K. Law, On flame-front instability at elevated pres-  
23 sures, *Proc. Combust. Inst.* 31 (2007) 1267–1274.
- 24 [48] F. Creta, P. E. Lapenna, R. Lamioni, N. Fogla, M. Matalon, Propagation  
25 of premixed flames in the presence of Darrieus–Landau and thermal  
26 diffusive instabilities, *Combust. Flame* 216 (2020) 256–270.
- 27 [49] T. Howarth, A. Aspden, An empirical characteristic scaling model for  
28 freely-propagating lean premixed hydrogen flames, *Combust. Flame* 237  
29 (2022) 111805.
- 30 [50] L. Berger, A. Attili, H. Pitsch, Synergistic interactions of thermodif-  
31 fusive instabilities and turbulence in lean hydrogen flames, *Combust.*  
32 *Flame* 244 (2022) 112254.

- 1 [51] S. Kadowaki, T. Hasegawa, Numerical simulation of dynamics of pre-  
2 mixed flames: flame instability and vortex–flame interaction, *Prog. En-  
3 ergy Combust. Sci.* 31 (3) (2005) 193–241.
- 4 [52] M. Faghiih, W. Han, Z. Chen, Effects of soot diffusion on premixed  
5 flame propagation under engine-relevant conditions, *Combust. Flame*  
6 194 (2018) 175–179.